Observations of the Liquid-Crystal Analog of the Abrikosov Phase

K. J. Ihn, J. A. N. Zasadzinski,* R. Pindak, A. J. Slaney, J. Goodby

Freeze-fracture transmission electron micrographs of the smectic A* phase confirm the twist grain boundary model of Renn and Lubensky. The fracture surface has an undulating structure with a 0.5-micrometer helical pitch parallel to 4.1-nanometer smectic layers. The layers are disrupted by a lattice of screw dislocations oriented normal to the helical axis. Optical diffraction shows that rotation of smectic blocks occurs in discrete steps of about 17°; hence, the screw dislocations are 14 to 15 nanometers apart and the grain boundaries are 24 nanometers apart. These observations show that the SmA* phase is the liquid-crystal analog of the Abrikosov phase in superconductors.

The discovery of a new liquid-crystal phase [called smectic-A* (SmA*)] that combines helical twist and smectic layering (*1–3*) was a surprise, as the classical description of the smectic phase precludes bend and twist distortions (*4*). However, preceding this discovery, the twist grain boundary (TGB) model of Renn and Lubensky (*5*) predicted a defect-mediated smectic phase that incorporates helical twist by a lattice of screw dislocations. The TGB model extends the analogy between superconductors and smectic liquid crystals first recognized by de Gennes (*6, 7*). The application of a twist distortion to smectic layers is analogous to the application of a magnetic field to a superconductor. In superconductors, the magnetic field is either expelled (type-I behavior) or incorporated into a lattice of flux vortices known as the Abrikosov flux lattice (type-II behavior) (*8*). The TGB model for the liquid-crystal analog of the Abrikosov phase consists of regularly spaced grain boundaries of screw dislocations that are parallel to each other within each grain boundary but are rotated by a fixed angle with respect to screw dislocations in adjacent grain boundaries. The screw dislocations divide the smectic layers into blocks that are rotated relative to adjoining blocks by a discrete amount, $\Delta\Psi$, given by the ratio of the layer thickness, d, to the separation between screw dislocations, ℓ_d; $\Delta\Psi \approx d/\ell_d$ (see Fig. 1) (*5*). This rotation results in a macroscopic helical structure, with the twist confined to grain boundaries and the layering preserved within each smectic block. The separation between grain boundaries is also simply related to the discrete twist; $\ell_b = \lambda_0\Delta\Psi/2\pi$, where λ_0 is the pitch of the helical twist (*5*).

The SmA* phase is found between the isotropic liquid and the smectic-C* (SmC*) phase in a homologous series of (*R*)- and (*S*)-enantiomers of 1-methylheptyl 4′-{[(4″-*n*-alkoxyphenyl)propioloyl]oxy}biphenyl-4-carboxylates (*n*P1M7) with n from 13 to 15 (*1–3*). The tetradecyl compound (+14P1M7) examined here has an SmC* to SmA* transition at 90°C and an SmA* to isotropic transition at 94°C (*1, 2, 9*). Optical measurements show a helical structure with a pitch that decreases from about 0.6 μm at 90°C to about 0.4 μm at 94°C (*9*). X-ray diffraction has shown that the layer spacing is constant over the SmA* phase and is about 4.3 nm, equivalent to the fully extended length of +14P1M7, and that the layers are parallel to the pitch axis (*1, 2, 9*). Although these observations are consistent with the TGB model for the SmA* phase, these results cannot distinguish between microscopic models for the molecular organization. Optical and x-ray techniques cannot detect screw dislocations or the discrete twist between blocks of smectic layers that are critical to the TGB model (*1, 2*). The details of the molecular organization of the SmA* phase are especially interesting because this phase belongs to a larger class of "frustrated" materials that are characterized by a competition between a preferred local packing and an allowable long-range or global order. Other frustrated materials include ripple phases of phospholipids (*10, 11*) and Langmuir-Blodgett films (*12*), quasi-crystals of rapidly cooled alloys (*13–15*), and blue phases of cholesteric liquid crystals (*16–20*).

Freeze-fracture transmission electron microscopy (TEM) is essential to visualizing the SmA* phase at sufficient resolution to resolve the molecular organization. This preparation technique can preserve the high-temperature structure without artifact (*18–23*). Our images show that the layers of the SmA* phase are disrupted by a large number of screw dislocations, which are oriented normal to the helical axis direction. Optical diffraction from the TEM negatives show that the layer spacing is approximately 4.1 nm and that the rotation of blocks of smectic layers along the helix occurs in discrete steps of roughly 17° between adjacent blocks. This implies that the screw dislocations are 14 to 15 nm apart and the grain boundaries are about 24 nm apart.

To prepare the SmA* phase for freeze-fracture replication, it must be quenched rapidly enough that the desired phase supercools and is frozen in place. As the SmC* phase forms by nucleation from the SmA* phase on cooling in +14P1M7, the transition can be avoided by rapid freezing (*18–23*). A 0.1- to 0.5-μl drop of +14P1M7 heated to >95°C was sandwiched between two copper planchettes (Balzers BUO-12-056T; Hudson, New Hampshire) coated with poly(1,4-butylene terephthalate) and unidirectionally buffed, although the alignment procedure did not influence the fracture (*24*). The thickness of the sample was not controlled and varied from about 10 to 50 μm. The sample sandwich was placed in a Mettler variable-temperature microscope stage next to a sample of +14P1M7 between two cover glass slides. The latter sample was observed through the polarizing microscope, and the stage temperature was adjusted to 92.5°C. At this temperature, the desired phase was identified optically, and the copper–liquid-

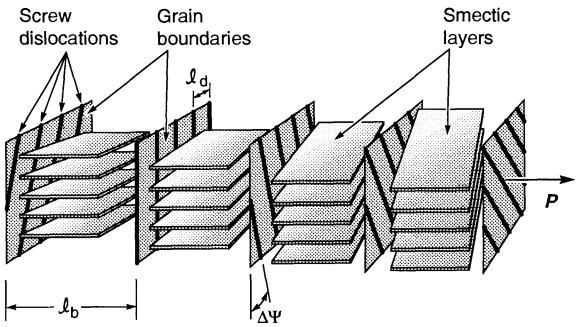

Fig. 1. Schematic representation of the TGB model of the SmA* phase. Blocks of SmA* layers of spacing d are separated by regularly spaced twist grain boundaries separated by a distance ℓ_b. The distance between screw dislocations within a grain boundary is ℓ_d. The angles of the normal to the smectic planes separated by a grain boundary differ by $\Delta\Psi \approx d/\ell_d$. The molecular director $n(z)$ lies in planes perpendicular to the pitch axis, $\hat{P}$. The director executes one full turn in a distance equal to the pitch, λ_0. The pitch is related to the distance between grain boundaries by $\lambda_0 = 2\pi\ell_b/\Delta\Psi$. The average configuration of the director in the TGB model is very similar to that of the cholesteric phase.

K. J. Ihn and J. A. N. Zasadzinski, Department of Chemical and Nuclear Engineering, University of California, Santa Barbara, CA 93106.
R. Pindak, AT&T Bell Laboratories, Murray Hill, NJ 07974.
A. J. Slaney and J. Goodby, School of Chemistry, The University, Hull, HU6 7RX, England.
*To whom correspondence should be addressed.

crystal sandwich was quickly plunged into liquid propane cooled to −190°C by liquid nitrogen. Cooling rates are about 5000°C per second (*23*). The quenched samples were fractured at −170°C and 10^{-8} torr in a Balzers 400 freeze-etch apparatus and replicated with a 1.5-nm-thick shadowing film of platinum deposited at a 45° angle with respect to the fracture surface, followed by a 15-nm-thick film of carbon deposited normal to the fracture surface. The replicas were removed from the copper planchettes and cleaned as described elsewhere (*25*), then examined in a JEM 100CXII transmission electron microscope operated at 80 kV; the images were recorded on Kodak SO163 film. Shadows (absence of platinum) appear light on the prints. We obtained optical Fourier transforms by spreading the beam of an He-Ne laser to about 1 cm and passing the beam through an area corresponding to roughly 0.25 to 1 μm^2 on the TEM negatives and recording the diffraction pattern on Polaroid film (*23*). The Q spacings ($Q = 2\pi/d$) were calibrated relative to optical transforms of images of catalase crystals taken at similar magnification (*23*).

A typical fracture pattern of the SmA* phase (Fig. 2A) shows that the surface has a regular asymmetric undulating texture similar to that observed in helical cholesteric liquid-crystal phases (*18, 19, 22*), and in agreement with the surface contours predicted by a simple model of a cholesteric fracture surface (*20*). The helical axis is oblique to the fracture plane (see below). From measurements of this and other images (not shown), the minimum undulating repeat distance is 0.25 to 0.30 μm (corresponding to one-half pitch); hence, the pitch is about 0.5 to 0.6 μm, which is consistent with optical measurements (*9*). However, in addition to the undulations, there is a discrete layering visible at the arrows. These are the smectic layers, and they are parallel to the helical axis, as shown by x-ray diffraction (*1, 2, 9*) and as predicted by the TGB model (*5*). At the bottom of each trough of the undulating fracture surface (open arrow), the layers are roughly normal to the fracture direction, and the 4.1 ± 0.3 nm spacing measured by optical diffraction from the TEM negative (Fig. 3) is consistent with the layer spacing observed by x-ray diffraction (*9*). Near the crest of the undulations, the layers are almost parallel to the fracture surface, and the fracture has the typical pattern of a dense array of screw dislocations (*22, 26*). These dislocations are oriented normal to the fracture surface and hence are perpendicular to the helical axis. A higher magnification view of an adjacent area (Fig. 2B) shows an oblique fracture through roughly one-half of a pitch, with the pitch axis roughly horizontal. On the right side of the figure, the layers are oriented normal to the fracture and the layer periodicity is visible. The "layer spacing" appears to change in distinct bands from left to right. Near the center of the figure, the layers are almost parallel to the fracture. The arrows mark the location of some of the screw dislocations that make up one of the twist grain boundaries. The screw dislocations are spaced roughly every 15 nm and have a Burgers vector of a single layer, which is expected from elastic energy considerations (*26*).

Optical transforms of selected 0.25 to 1.0 μm^2 areas of Fig. 2A (Fig. 3) show a distinctive "bow-tie" pattern of diffuse scattering that is typical for unidirectionally shadowed freeze-fracture micrographs (other areas of Fig. 2A and other micrographs show similar patterns) (*23, 27*). Superimposed on the diffuse scattering are several pairs of Bragg-like reflections. The weak reflections, at the tips of the arrows, farthest from the center correspond to a spacing of 4.1 ± 0.3 nm, which is consistent with the known smectic layer spacing. The additional pairs of reflections (numbered 2 to 6 in Fig. 3A and 2 to 4 in Fig. 3B) correspond to longer spacings in the image, which are rotated by an angle Ψ' from the first set of spots. The reflections indicate that the apparent layer spacing changes discontinuously along the helical axis, which proves that the fracture plane cuts discretely rotating blocks as predicted by the TGB model of the SmA* phase as shown in Fig. 4.

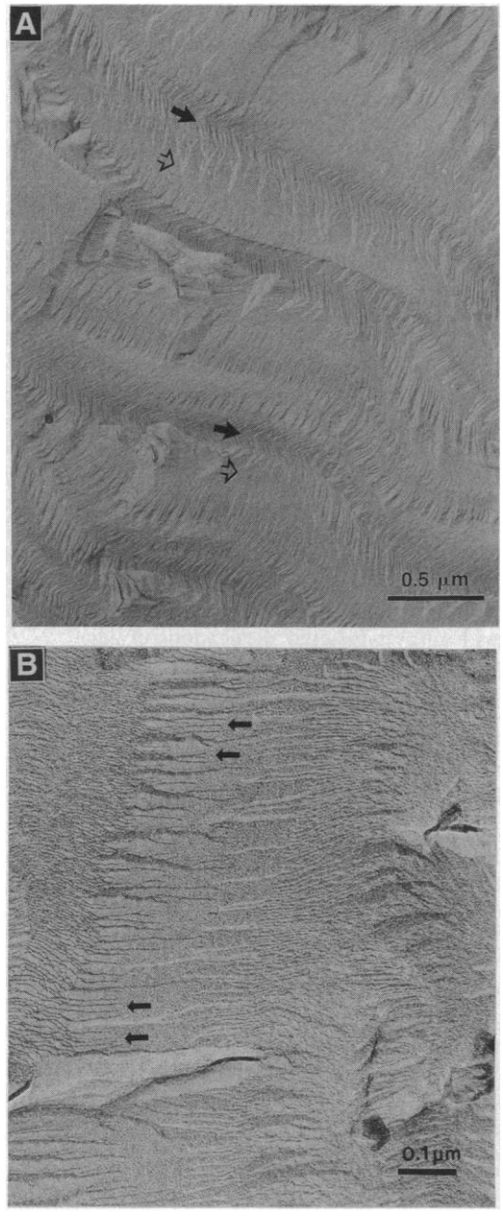

Fig. 2. (**A**) Freeze-fracture morphology of the SmA* phase of +14P1M7 quenched from 92.5°C. The overall fracture pattern has a regular undulating texture similar to the fracture patterns of cholesteric liquid crystals (*18–22*). The projection of the helical axis onto the fracture plane is roughly vertical in the picture, and surface features repeat about every 0.3 to 0.5 μm. Discrete layers are visible at the arrows that are parallel to the helical axis (roughly vertical) as predicted by the TGB model. At the open arrows, the layers are normal to the fracture plane and the 4.1 ± 0.3 nm spacing measured by optical diffraction is consistent with the layer spacing observed by x-ray diffraction. At the full arrows, the layers are almost parallel to the fracture surface, and the fracture steps that are visible are the signature fracture pattern of a dense array of screw dislocations oriented normal to the fracture surface and the smectic layers and hence perpendicular to the helical axis. (**B**) Freeze-fracture image of typical screw dislocations in the SmA* phase. The characteristic "river" fracture pattern, which terminates abruptly at the defect core, is characteristic of screw dislocations (arrows) [also see figures 5.19 to 5.21 in (*26*)]. From measurements of the shadow width, we conclude that these screw dislocations have a Burgers vector of a single layer step, which is predicted by elastic energy considerations, and is consistent with the TGB model. The screw dislocations form the twist grain boundaries that cause the orientation of the layers to change abruptly with respect to the fracture surface in roughly vertical bands from left to right. The dislocations are spaced about 15 nm apart. (Only the dislocations roughly normal to the fracture surface at the arrows are easily visible in the image.) The apparent layer spacing changes in discrete vertical bands from right to left, as in the TGB model in Fig. 1 and the fracture surface model in Fig. 4A.

Figure 4A shows a wedge cut from a particular TGB structure that has a rotation angle $\Delta\Psi = 15°$. In the "uncut" TGB structure, the layer blocks extend uninterrupted except for the screw dislocation planes (see Fig. 1). The front surface of the wedge illustrates how the TGB layers intersect a plane that contains the pitch axis, $\hat{P}$; the upper surface of the wedge illustrates how the TGB layers intersect a planar fracture surface (taken to be the xy plane) with a surface normal 60° from the pitch axis. In the leftmost block of the wedge, the layers are perpendicular to the $x\hat{P}$ plane and intersect the xy fracture surface in an infinite set of finite length "lines" oriented parallel to the y axis and separated by the smectic layer spacing, d. In contrast, in the rightmost block of the wedge, the layers are parallel to the $x\hat{P}$ plane and intersect the xy fracture surface in only a few "lines" oriented parallel to the x axis and spaced by a distance $d/\cos(60°) = 2d$. The "lines of intersection" of the layers with the fracture surface for the intermediate blocks are between these two extremes in both their orientation and spacing. Hence, if we neglect finite size effects, for this 60° surface fracture the first-order diffraction pattern from the layer "lines of intersection" is a discrete set of spots located on an ellipse with major and minor axes $2\pi/d$ and π/d, respectively.

The reciprocal-space diagram for the general case of pitch axis, $\hat{P}$, oriented in an arbitrary direction (θ,ϕ) with respect to the fracture surface is illustrated in Fig. 4B. The periodicity of the TGB structure is described by a "circle" of reciprocal **Q** vectors (one per block) of magnitude $Q_0 = 2\pi/d$ and oriented normal to $\hat{P}$ and at an angle Ψ with respect to the line of intersection of the "circle" with the xy plane. The a axis in Fig. 4B is along this line of intersection. Fracturing the TGB structure parallel to the xy plane results in a structure (similar to the fracture surface in Fig. 4A) whose periodicities are determined by projecting the TGB "circle" of reciprocal **Q** vectors onto the xy fracture plane. It is evident from Fig. 4B that this projection is an ellipse with its major axis along $\hat{a}$ and minor axis along a direction $\hat{b}$ in the xy plane perpendicular to $\hat{a}$. The following relations can then be derived relating the TGB reciprocal vectors, $\mathbf{Q}(\Psi)$, to the reciprocal vectors, $\mathbf{Q}'(\Psi')$, associated with its projection onto the fracture surface:

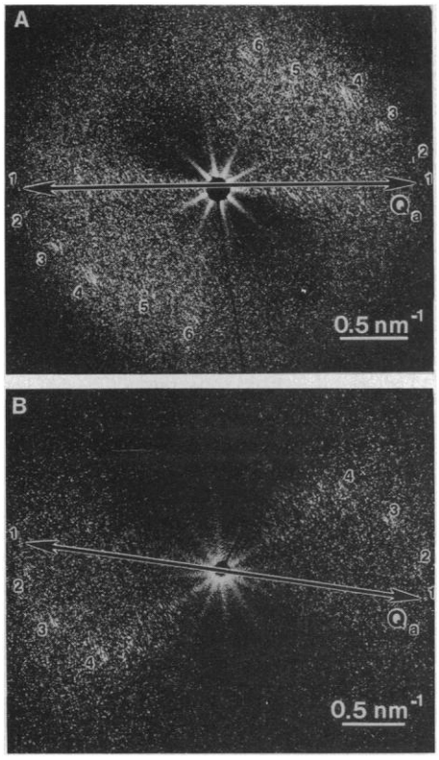

Fig. 3. (**A**) Optical diffraction pattern of a selected area near the center of Fig. 2A. The optical transform shows an asymmetric diffuse background and six pairs of Bragg-like reflections. The pair of reflections farthest from the origin corresponds to a spacing of 4.1 ± 0.3 nm, which corresponds to the smectic layer spacing. The line connecting these reflections is along the axis labeled $\hat{a}$, and the reflections are located at the intersection of Q and Q' on $\hat{a}$ in Fig. 4B. The angular dependence of the diffuse scattering is proportional to $\sin^2(\mathbf{Q}/2\cdot\mathbf{s})$, where **Q** is the scattering vector and **s** is a vector in the direction of the metal shadowing with length proportional to the shadowing layer thickness. When **Q** is perpendicular to **s**, there is no information about the contours of the fracture surface in the image, and the scattering is zero. For these images, $|s|$ is about 1 nm and is oriented roughly from bottom left to top right. (**B**) Optical diffraction pattern of a selected area at the upper right of Fig. 2A. This optical transform reveals four pairs of spots, again with the pair of spots farthest from the origin corresponding to a spacing of 4.1 nm. (The ten-armed star at the center surrounding the beam stop is due to the selected area aperture used.)

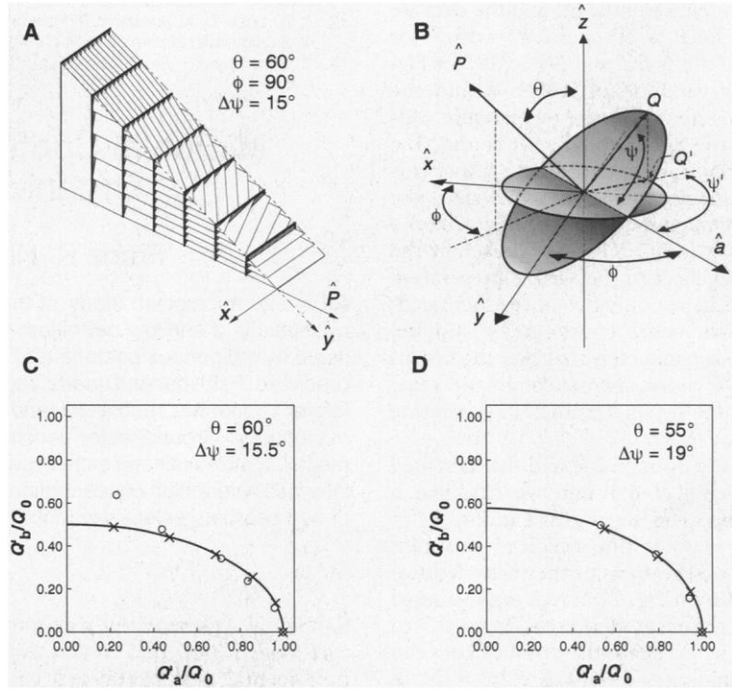

Fig. 4. (**A**) Wedge cut from the TGB structure illustrating how the TGB layers intersect a planar fracture surface. The fracture surface is taken to be the xy plane and its surface normal makes a 60° angle with respect to the TGB pitch axis, $\hat{P}$. The rotation angle between layer blocks, $\Delta\Psi$, is 15°. (**B**) Reciprocal-space diagram of the "circle" of **Q** vectors describing the periodicities of the TGB structure as well as the "ellipse" of **Q′** vectors describing the intersection of the TGB layers with the xy fracture surface. The angles θ and ϕ specify the orientation of the TGB pitch axis with respect to the xy fracture surface. The Q_a axis (Fig. 3) is the line defined by the intersection of the circle of **Q** vectors and the xy plane. (**C** and **D**) Plots of the measured **Q′** vectors taken from the optical diffraction patterns in Fig. 3, A and B, respectively. The **Q′** vector components have been normalized by $Q_0 = 2\pi/d = 1.53\ \text{nm}^{-1}$, where d is the smectic layer spacing. The open circles are the experimental points, and the solid lines are fits to the ellipses generated from Eqs. 1 and 2. The "best fit" values for the cut angle, θ, the angle between the pitch axis and the fracture surface normal, are indicated. The X's are points on these ellipses that correspond to the indicated, fixed block rotation angle, $\Delta\Psi$. Only the final point in Fig. 4C significantly deviates from the fit, most likely due to the nonplanar nature of the actual fracture.

$$Q' = Q_0[1 - \sin^2(\Psi)\sin^2(\theta)]^{1/2} \quad (1)$$

$$Q'\cos(\Psi') = Q_0\cos(\Psi) \quad (2)$$

In Fig. 4, C and D, the two sets of optical diffraction spots, from Figs. 3A and 3B, respectively, are shown fit to ellipses given by Eqs. 1 and 2. The open circles are the experimental points. Because, in each data set, the magnitude of the scattering vectors for the spots with the largest spacing were approximately $2\pi/d = 1.53$ nm^{-1}, these spots were taken to define the Q_a axis. The points in Fig. 4C closest to the Q'_b axis correspond to diffraction from blocks similar in orientation to the rightmost blocks in Fig. 4A. The intersection of the fracture surface with these blocks results in only a few layer "lines," and the resulting diffraction features were either diffuse (Fig. 3A) or unobservable (Fig. 3B). The ×'s in Fig. 4, C and D, are the expected locations of the optical diffraction spots for a constant rotation angle between layer blocks of $\Delta\Psi$. Except for the single point in Fig. 4C near the Q'_b axis (which corresponds to one of the weakest diffraction features), excellent agreement between the fits and the data are obtained for $\theta = 60°$ and $\Delta\Psi = 15.5°$ for Fig. 4C and $\theta = 55°$ and $\Delta\Psi = 19°$ for Fig. 4D. This variation in $\Delta\Psi$ is within the range consistent with the temperature variation of the helical pitch. Of course, the real fracture surface is not planar, but this idealized fracture closely approximates the optical diffraction. [The symmetry of the optical transforms in Fig. 3 is broken by the shadowing effect of the sample preparation (*27*), and hence only two of the four quadrants of the ideal transform are visible.] Finally, the parameters that give the best fit in Fig. 4C have approximately the same values as the parameters used in generating Fig. 4A.

From the average $\Delta\Psi$ and the measured layer spacing of 4.1 nm, we calculate a spacing between screw dislocations, $\ell_d \approx d/\Delta\Psi = 14$ to 15 nm, which is consistent with our observations of the screw dislocation density in Fig. 2B. From our measured $\Delta\Psi$ and the measured pitch, $\lambda_0 \approx 0.5$ to 0.6 μm, we estimate the distance between grain boundaries, $\ell_b \approx \lambda_0\Delta\Psi/2\pi = 24$ to 28 nm.

Our freeze-fracture results give clear evidence that the TGB model is a good description of the SmA* phase. The images show a regular undulating cholesteric-like structure with a length scale of 0.5 to 0.6 μm, consistent with a macroscopic helical pitch, and simultaneously show the smectic layering with a spacing of 4.1 nm. In addition, we see the characteristic fracture pattern of a high density of elementary screw dislocations oriented normal to the twist axis. Optical diffraction shows that the layers twist in discrete steps of about 17°, dictating that the screw dislocations are spaced every 14 to 15 nm and there is about 24 nm between grain boundaries. This combination of evidence, which is unobtainable by any other technique, clearly shows that the SmA* phase is the liquid-crystal analog of the Abrikosov phase in superconductors and completes the analogy between smectic phases and superconductors as given by the TGB model.

REFERENCES AND NOTES

1. J. W. Goodby *et al.*, *Nature* **337**, 449 (1989).
2. J. W. Goodby *et al.*, *J. Am. Chem. Soc.* **111**, 8119 (1989).
3. A. J. Slaney and J. W. Goodby, *J. Mater. Chem.* **1**, 5 (1991).
4. F. C. Frank, *Disc. Faraday Soc.* **25**, 19 (1958).
5. S. R. Renn and T. C. Lubensky, *Phys. Rev. A* **38**, 2132 (1988).
6. P. G. de Gennes, *Solid State Commun.* **10**, 753 (1972).
7. ———, *Science* **256**, 495 (1992).
8. A. A. Abrikosov, *Sov. Phys. JETP* **5**, 1174 (1957).
9. G. Srajer, R. Pindak, M. A. Waugh, J. W. Goodby, J. S. Patel, *Phys. Rev. Lett.* **64**, 1545 (1990).
10. J. M. Carlson and J. P. Sethna, *Phys. Rev. A* **36**, 3359 (1987).
11. J. A. N. Zasadzinski, J. Schneir, J. Gurley, V. Elings, P. K. Hansma, *Science* **239**, 1013 (1988).
12. J. Garnaes, D. K. Schwartz, R. Viswanathan, J. A. N. Zasadzinski, *Nature* **357**, 54 (1992).
13. D. Schectman, I. Blech, D. Gratias, J. W. Cahn, *Phys. Rev. Lett.* **53**, 1951 (1984).
14. N. D. Mermin and S. M. Troian, *ibid.* **54**, 1525 (1985).
15. P. A. Kalugin, A. Yu. Kitaev, L. S. Levitov, *JETP Lett.* **41**, 145 (1985).
16. S. Meiboom, J. P. Sethna, P. W. Anderson, W. F. Brinkman, *Phys. Rev. Lett.* **46**, 1216 (1981).
17. J. P. Sethna, *Phys. Rev. B* **31**, 6278 (1985).
18. M. J. Costello, S. Meiboom, M. J. Sammon, *Phys. Rev. A* **29**, 2957 (1984).
19. J. A. N. Zasadzinski, S. Meiboom, M. J. Sammon, D. W. Berreman, *Phys. Rev. Lett.* **57**, 364 (1986).
20. D. W. Berreman, J. A. N. Zasadzinski, M. J. Sammon, S. Meiboom, *ibid.*, p. 1737.
21. M. J. Sammon, J. A. N. Zasadzinski, M. Kuzma, *ibid.*, p. 2834.
22. J. A. N. Zasadzinski, *J. Phys.* (*Paris*) **51**, 747 (1990).
23. ——— and S. M. Bailey, *J. Electron. Microsc. Tech.* **13**, 309 (1989).
24. J. Patel, T. M. Leslie, J. W. Goodby, *Ferroelectrics* **57**, 137 (1984).
25. K. J. Ihn and J. A. N. Zasadzinski, in preparation.
26. M. Kléman, *Points, Lines, and Walls* (Wiley, Chichester, England, 1983), chap. 5.
27. D. L. Misell, in *Image Analysis, Enhancement and Interpretation*, vol. 7 of *Practical Methods in Electron Microscopy*, A. M. Glauert, Ed. (North-Holland, Amsterdam, 1978), chap. 4.

28. We thank J. Patel for suggestions on orienting the smectic samples. K.J.I. and J.A.N.Z. acknowledge financial support from the Whitaker Foundation Biomedical Engineering grant, the Donors of the Petroleum Research Fund, and the National Science Foundation under grants CBT86-57444 and CTS90-15537.

5 May 1992; accepted 20 July 1992

Microbial Control of Silicate Weathering in Organic-Rich Ground Water

Franz K. Hiebert and Philip C. Bennett

An in situ microcosm study of the influence of surface-adhering bacteria on silicate diagenesis in a shallow petroleum-contaminated aquifer showed that minerals were colonized by indigenous bacteria and chemically weathered at a rate faster than theoretically predicted. Feldspar and quartz fragments were placed in anoxic, organic-rich ground water, left for 14 months, recovered, and compared to unreacted controls with scanning electron microscopy. Ground-water geochemistry was characterized before and after the experiment. Localized mineral etching probably occurred in a reaction zone at the bacteria-mineral interface where high concentrations of organic acids, formed by bacteria during metabolism of hydrocarbon, selectively mobilized silica and aluminum from the mineral surface.

Chemical weathering of rock-forming silicate minerals at the Earth's surface is a fundamental process and is a basis of the global geochemical cycling of the elements (*1*). Silicate solubility and aqueous dissolution kinetics are reasonably well characterized and are known to be controlled by many variables, including crystal lattice defects, solution pH, temperature, ionic strength, and the presence or absence of inorganic and organic ligands (*2*). The role of microbes is rarely factored into models of subsurface rock-water interactions, even though silicates dissolve faster in microbially active organic-rich waters than predicted by estimates made on the basis of the bulk ground-water geochemical environment (*3*, *4*).

In the pH range of most natural waters, silicate dissolution is extremely slow (*2*). In the absence of complexing ligands, silica (SiO_2) is released from microcline at pH 7 and at 25°C at a rate of about $10^{-15.5}$ mol cm^{-2} s^{-1}. Under similar conditions, quartz dissolves at a rate of $10^{-16.5}$ mol cm^{-2} s^{-1} (*5*, *6*). Organic electrolytes, especially organic acids, accelerate the dissolution of feldspar at mildly acidic pH by surface complexing of metals that speed the breakdown of framework metal-oxygen bonds, which is considered the rate-limiting step

Department of Geological Sciences, The University of Texas at Austin, Austin, TX 79713.